Journal of Materials Chemistry B

ROYAL SOCIETY OF CHEMISTRY

PAPER

View Article Online
View Journal

Cite this: DOI: 10.1039/d0tb00201a

Engineering one-dimensional trough-like Au–Ag_2S nano-hybrids for plasmon-enhanced photoelectrodetection of human α-thrombin†

Wen-Chao Geng,[a] De-Lin Li,[a] Ji-Long Sang,[a] Liang-Liang Pan,[a] Ze-Li Jiang,[a] Cai Liu*[b] and Yong-Jun Li *[a]

One-dimensional (1D) morphology-unique Au–Ag_2S nano-hybrids are achieved by combining the interfacial self-assembly of Ag nanowires, interface-oriented site-specific etching of Ag nanowires with $AuCl_4^-$, and the sulfurization of S^{2-}. The as-formed Au–Ag_2S nano-hybrid has a trough-like morphology. The wall of the Au–Ag_2S nanotrough is a Ag_2S/Au/Ag_2S trilayer wall, but the Ag_2S layer is a Ag_2S-rich mixture of Ag_2S and Au rather than pure Ag_2S because of the diffusion of Au atoms towards Ag_2S. The Au–Ag_2S nanotrough shows strong absorption in the visible region (400–800 nm) and exhibits a favorable photoelectrochemical (PEC) response, the photocurrent of which is ~8.5 times larger than that of pure Ag_2S. This enhanced PEC response originates from the localized plasmonic resonance effect of Au. Moreover, the PEC biosensor based on the Au–Ag_2S nanotroughs shows high sensitivity and selectivity, satisfactory reproducibility, and good stability towards human α-thrombin (TB) detection: a sensitive linear response ranging from 1.00 to 10.00 pmol L^{-1} and a low detection limit of 0.67 pmol L^{-1}. This study provides a new model for studying the PEC behavior of plasmonic metal/semiconductor materials, and this Au–Ag_2S nanotrough may also be useful in the fields of photocatalysis and photovoltaics.

Received 21st January 2020,
Accepted 1st July 2020

DOI: 10.1039/d0tb00201a

rsc.li/materials-b

1 Introduction

Photoelectrochemical (PEC) sensors show broad prospects for commercial applications because of their high sensitivity, easy electronic readout, and feasible miniaturization.[1,2] Semiconductors as traditional PEC active materials have been widely investigated, such as CdTe,[3] TiO_2,[4] Bi_2S_3,[5] ZnO,[6] C_3N_4,[7] and Ag_2S.[2] Among these semiconductors, TiO_2 is one of the most frequently employed materials owing to its high stability, low cost, nontoxicity, and strong oxidizing power.[8] However, TiO_2 is a typical wide-bandgap semiconductor (~3.2 eV),[4] which only responds to high-energy UV light. UV light accounts for only ~3–5% of sunlight energy,[9] far less than that of visible light (~42–45%),[8] and it is usually harmful to biomolecules.[10,11] Thus, developing visible-near-IR photoactive materials may efficiently increase the utilization of sunlight energy and favor bio-analytical detection. In terms of this concept, narrow-bandgap semiconductors (*e.g.*, CdS,[12] CdSe,[13] Ag_2S,[2] and PbS[14]), easily irradiated by visible-near-IR light,[12,15] may be superior to the wide-bandgap ones. Unfortunately, narrow-bandgap semiconductors always suffer from the rapid recombination of the photogenerated electron/hole (e^-/h^+), resulting in a weak PEC response.[12]

Many investigations[13–15] demonstrate that engineering plasmonic metal/semiconductor hetero-junctions can enhance the PEC response of narrow-bandgap semiconductors. Under specific light illumination, the surface-enhanced scattering effect of plasmonic metals can increase the optical absorption of semiconductors;[16,17] on the other hand, the localized surface plasmon resonance (LSPR) effect of plasmonic metals can promote the separation of photogenerated e^-/h^+ pairs of the semiconductor by injecting e^- to the semiconductor[18] or extracting e^- from the semiconductor[7] (depending on the alignment of the energy bands of the semiconductor and Fermi energy level of the metal[19]). Besides, if there is some overlap between the LSPR spectrum of the metal and the absorption band of the semiconductor, the plasmonic resonant energy transfer from metal to semiconductor also benefits the generation of e^-/h^+ pairs in the semiconductor and thus enhances the PEC response.[18,20] For example, the photocurrent of multi-segmented CdS–Au nanorod arrays is twice that of pure CdS nanorod arrays,[21] showing excellent photocatalytic performance in hydrogen evolution reaction.

[a] State Key Lab of Chemo/Biosensing and Chemometrics, College of Chemistry and Chemical Engineering, Hunan University, Changsha 410082, China. E-mail: liyje@hnu.edu.cn
[b] College of Chemical Engineering, Beijing Institute of Petrochemical Technology, Beijing 102617, China. E-mail: liucai@bipt.edu.cn

† Electronic supplementary information (ESI) available. See DOI: 10.1039/d0tb00201a

Narrow-bandgap semiconductors involving toxic elements such as Cd and Pb are unsuitable for practical applications,[22] especially for bio-analytical detection.[23] Among various environment-friendly narrow-bandgap semiconductors, Ag_2S (the bandgap, $\sim$1.0 eV) is a representative and has been widely used in photocatalysis,[24] bioimaging,[25] and PEC biosensing,[18] thanks to its chemical stability, high optical absorption coefficient, and easy preparation.[26] To improve the PEC performance of Ag_2S, plasmonic metals (*e.g.*, Cu, Ag and Au) have been used to fabricate hetero-junctions of Cu–Ag_2S,[27] Ag–Ag_2S,[28,29] and Au–Ag_2S,[30,31] where Au is frequently preferred owing to its wide absorption in the visible-near-IR region, chemical stability, and good biocompatibility.[18] More importantly, most reported Au–Ag_2S heterostructures exhibit enhanced photosensitive activity.[18,30,32,33] For example, a Ag_2S nanostructured film modified by Au nanoparticles shows $\sim$2.5 times the photoelectric conversion efficiency of the pure Ag_2S film.[18]

Besides, the PEC performance of a plasmonic metal/semiconductor composite is closely linked to its morphology. The one-dimensional (1D) hollow nanostructure possesses a large surface area, capable of providing abundant active sites[34,35] and thus producing a strong photocurrent signal. Also, a 1D geometry can enhance light absorption relative to its 0D counterpart,[36] facilitating the photo-generation of the e^-/h^+ pair and its transport along the 1D nanostructure. Thus, rationally designing a 1D hollow Au–Ag_2S nanostructure may be an effective way to improve PEC performance. However, to the best of our knowledge, the existing Au–Ag_2S PEC active materials usually have core–shell,[31,37] Janus,[38] and bilayer[18] architectures, and these well-defined architectures cannot maximize the PEC performance of Au–Ag_2S because of their 0D morphologies and the limited contact area between Au and Ag_2S.[39,40]

Herein, inspired by the finding that Au and Ag_2S are mutually soluble under a certain condition,[31] we achieve the formation of a 1D Au/Ag_2S core/shell-like heterostructure and double the contact area of Au and Ag_2S by one-step sulfurization of the AgAu alloy nanotrough with an ultrathin wall. The 1D Au/Ag_2S core/shell-like heterostructure still has a trough-like morphology, and acting as a PEC material, it shows a larger photocurrent and a lower charge-transfer resistance than that of pure Ag_2S. Also, this Au–Ag_2S PEC biosensor has a sensitive linear response range (1.00–10.00 pmol L^{-1}) and a low detection limit (*i.e.*, 0.67 pmol L^{-1}) towards the detection of human α-thrombin, completely meeting the practical requirements.

2 Experimental

2.1 Reagents

$AgNO_3$ ($\geq$99.8%), ethylene glycol ($\geq$99%), ethanol ($\geq$99.7%), $Na_2S{\cdot}9H_2O$ ($\geq$98%), and ascorbic acid (AA, $\geq$99%) were purchased from Sinopharm Chemicals Reagent Co. Ltd (China). Human α-thrombin (TB), bovine serum albumin (BSA), polyvinylpyrrolidone (PVP, MW $\approx$ 29 000), and $HAuCl_4{\cdot}3H_2O$, ($\geq$49.0% Au basis) were obtained from Sigma-Aldrich. DNA (*i.e.*, 5′-NH_2-$(CH_2)_6$-GGT TGG TGT GGT TGG-3′) was purchased from Sangon Biotechnology Co. Ltd (China). Tris-(hydroxymethyl) aminomethane (Tris) was purchased from Solarbio Science & technology Co., Ltd (China). All chemicals were used as received. Milli-Q water (18.2 MΩ cm) was used in all experiments. DNA and TB solutions of different concentrations were prepared by dissolving DNA and TB, respectively, in 20.0 mmol L^{-1} pH 7.4 Tris–HCl solution containing 140.0 mmol L^{-1} NaCl, 5.0 mmol L^{-1} KCl, 1.0 mmol L^{-1} $CaCl_2$, and 1.0 mmol L^{-1} $MgCl_2$.

2.2 Synthesis, interfacial self-assembly, and etching of Ag nanowires

Silver nanowires were prepared by using a previously reported polyol process (see ESI†).[41,42] The purified Ag nanowires were redispersed in ethanol (250 mL) for further use. Interfacial self-assembly and etching of Ag nanowires were performed according to our previously developed method[43] with minor modification. Briefly, a Ag nanowire solution (800 μL) was added into 2 mL of toluene under ultrasonication, into which was rapidly poured 7 mL of H_2O. A toluene/water interface was formed quickly, and meanwhile, a pale-yellow Ag nanowire monolayer appeared at the interface. After evaporation of toluene, $HAuCl_4$ aqueous solution (10 μL, 25.4 mmol L^{-1}) was injected into the water phase with a syringe, followed by 30 s of gentle stirring (tip: do not disturb the interfacial monolayer). After the system was maintained undisturbed for 12 h, interfacial Ag nanowires were transformed into 1D AgAu nanotroughs. Interfacial 1D AgAu nanotroughs can be transferred onto solid substrates for further use by a "touching and loading" method from the water phase.[42,43] Additionally, the interfacial 1D AgAu nanotroughs can be collected, washed with ethanol, and redispersed into ethanol or water.

2.3 Sulfurization of AgAu nanotroughs

The resulting 1D AgAu nanotroughs (4 mg) were redispersed into a Na_2S aqueous solution (10.0 mmol L^{-1}, 10 mL) and kept for 1 h. A black product (*i.e.*, 1D Au–Ag_2S nanotroughs) was collected by centrifugation, washed with water, and redispersed into H_2O (5 mL) for further use. The pure Ag_2S was also synthesized under the same conditions by redispersing Ag nanowires into a Na_2S aqueous solution.

2.4 Fabrication of PEC active electrode

An indium–tin oxide (ITO) glass disk (5.6 mm in diameter), prior to modification, was cleaned successively with acetone, an ethanol/water (v/v, 1 : 1) mixture containing 1.0 mol L^{-1} NaOH, and water under ultrasonication. After the cleaned ITO disk was dried in air, 25 μL of 1D Au–Ag_2S nanotrough aqueous solution was applied onto the ITO disk by a drop-coating method (Scheme 1a) and dried at room temperature. A Au–Ag_2S nanotrough-modified ITO electrode (ITO/Au–Ag_2S) was obtained.

To obtain the PEC active electrode, ITO/Au–Ag_2S was covered with DNA by adding 20 μL of 1.0 μmol L^{-1} DNA stock solution, and was kept at 4 °C for 12 h (Scheme 1b). The optimized DNA concentration was determined by assessing the correlation between the photocurrent of ITO/Au–Ag_2S/DNA and the concentration of

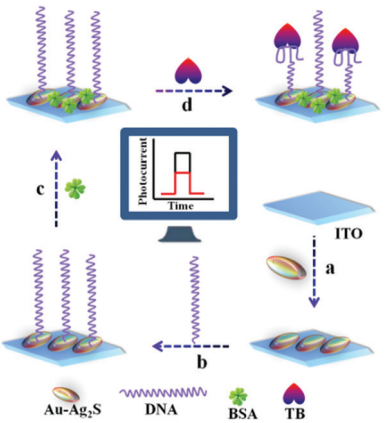

Scheme 1 Illustration of the fabrication of the ITO/Au–Ag_2S/DNA/BSA electrode for the detection of TB: (a) modification of Au–Ag_2S on ITO, (b) modification of DNA on ITO/Au–Ag_2S, (c) blocking of nonspecific binding sites of ITO/Au–Ag_2S/DNA with BSA, and (d) TB detection by assessing the photocurrent change (inset).

DNA (Fig. S1, ESI†). Subsequently, 20 μL of BSA aqueous solution (1.0 wt%) was added to block nonspecific binding sites (Scheme 1c). The as-fabricated PEC active electrode was designated as ITO/Au–Ag_2S/DNA/BSA. The successful modification of DNA and BSA was fully supported by electrochemical impedance spectroscopy (EIS) data (Fig. S2, ESI†).

2.5 Detection of human α-thrombin

TB detection was performed by immobilizing TB on the ITO/Au–Ag_2S/DNA/BSA electrode, that is, 20 μL of TB solution of different concentrations was added onto ITO/Au–Ag_2S/DNA/BSA, sealed and maintained at room temperature for 60 min to form the ITO/Au–Ag_2S/DNA/BSA/TB electrode (Scheme 1d). The 60 min reaction time was determined by optimization (Fig. S3, ESI†).

2.6 PEC and electrochemical measurements

PEC and electrochemical measurements were performed in a three-electrode configuration. ITO/Au–Ag_2S, ITO/Au–Ag_2S/DNA, ITO/Au–Ag_2S/DNA/BSA, or ITO/Au–Ag_2S/DNA/BSA/TB was used as the working electrode. Platinum wire and a saturated calomel electrode (SCE) were used as the auxiliary electrode and the reference electrode, respectively. All the potentials were referred to SCE unless otherwise specified. All PEC measurements were carried out in Tris–HCl (pH 7.4, 0.10 mol L^{-1}) buffer containing 0.10 mol L^{-1} ascorbic acid at 0 V.

2.7 Characterization and instrumentation

PEC and electrochemical measurements were carried out using a CHI 660D Electrochemical Workstation (Chenhua, Shanghai). A PLS-SXE300 xenon lamp was used as the excitation source ($\lambda > 420$ nm with an ultraviolet cutoff filter). Scanning electron microscopy (SEM) images were obtained on a JSM-6700F scanning electron microscope at 5 kV. Transmission electron microscopy (TEM) images were obtained on a JEM-3010 transmission electron microscope at 300 kV. X-ray photoelectron spectroscopy (XPS) measurement was conducted using a K-Alpha 1063 X-ray photoelectron spectrometer (Thermo Fisher Scientific) with an Al Kα X-ray source. High-resolution transmission electron microscopy (HRTEM), scanning transmission electron microscopy (STEM) and energy-dispersive X-ray spectroscopy (EDX) elemental mapping analysis were performed using a FEI Tecnai G2 F20 field emission TEM microscope. X-ray diffraction (XRD) patterns were obtained using a θ–2θ X-ray diffraction Siemens D5000 apparatus. UV-vis spectra were recorded on a UV-1800 spectrophotometer (Shimadzu). Photoluminescence (PL) spectra were obtained on a Hitachi F-4600 fluorescence spectrofluorometer (Tokyo, Japan), and the PL measurements were taken at an excitation wavelength of 550 nm.

3 Results and discussion

3.1 Characterization of one-dimensional AgAu and Au–Ag_2S nanotroughs

By employing our developed interfacial self-assembly strategy,[44] most Ag nanowires in solution can be arrested at a water/toluene interface. The interfacial Ag nanowires were parallel with each other, forming a close-packed monolayer (Fig. 1a and Fig. S4a, ESI†), and each nanowire had a smooth surface (Fig. 1a and c). After evaporation of toluene and injection of $AuCl_4^-$ into the water phase, smooth Ag nanowires were eventually transformed into 1D AgAu nanotroughs, that is, a deep trench was formed along the longitudinal axis of each nanowire (Fig. 1b and Fig. S4b, ESI†). Compared with the original Ag nanowire (Fig. 1c), the 1D AgAu nanotrough was more transparent (Fig. 1d). The wall of the AgAu nanotroughs has a sub-10 nm thickness, ~6–8 nm (Fig. 1d).

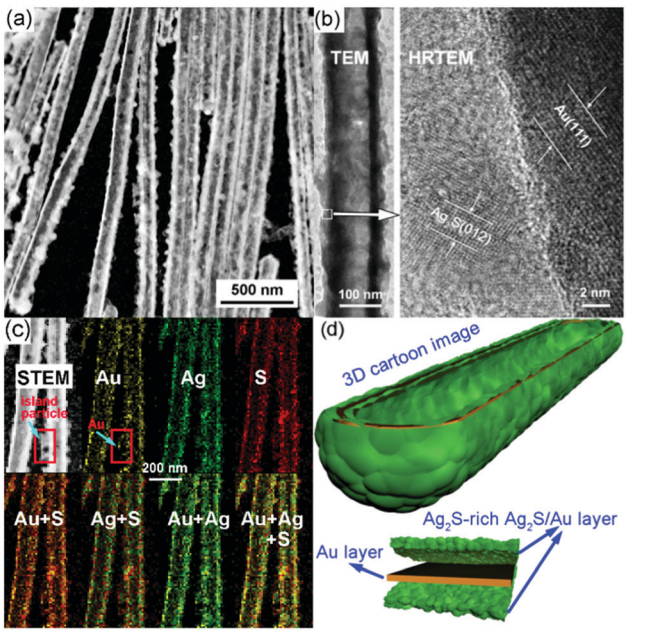

Fig. 1 (a) SEM images of interfacial Ag nanowire monolayer obtained *via* a two-phase interfacial assembly; (b) SEM image of 1D AgAu nanotrough monolayer evolved from the interfacial Ag nanowire *via* interface-oriented site-specific etching with $AuCl_4^-$, where the inset is the cartoon image of a 1D AgAu nanotrough; (c) and (d) TEM images of a Ag nanowire (c) and 1D AgAu nanotrough (d).

Additionally, the wall exhibited clear lattice fringes (Fig. S5, ESI†), and the neighboring lattice interspacing was 0.236 nm, corresponding to either Ag(111) (PDF#65-8428) or Au(111) (PDF#04-0784), indicative of its AgAu alloy feature (Fig. S6, ESI†), fully consistent with our previous report.[43]

After treatment in the Na_2S solution, the 1D AgAu nanotrough was transformed into a 1D Au–Ag_2S hybrid. Although the as-formed 1D Au–Ag_2S hybrid retained a nanotrough-like structure (Fig. 2a), many island-like particles appeared. The TEM image (Fig. 2b) shows that the inner and outside wall surfaces became much rougher than the original AgAu nanotrough (Fig. 1d) owing to the formation of Ag_2S. HRTEM analysis (Fig. 2b) reveals that the wall of the 1D Au–Ag_2S nanotrough was a Au/Ag_2S core/shell-like structure because Ag_2S dominated the inner and outside surfaces of the Au–Ag_2S nanotrough. This result indicates that, during the sulfurization process, the Ag component was extracted from the AuAg alloy along different directions and transformed into Ag_2S, leaving Au behind and forming a Au/Ag_2S core/shell-like structure. Because of the loose structure of Ag_2S and its lower density (7.20 g cm^{-3}) than that of Ag (10.51 g cm^{-3}), the apparent wall thickness of the Au–Ag_2S nanotrough (TEM in Fig. 2b) was obviously larger than that of the AuAg nanotrough (Fig. 1d), ~14 nm. This expansion effect has been observed in the previously reported sulfurization of Ag nanoprisms[28] and Ag nanocubes.[45]

STEM-EDX mapping images (Fig. 2c) show that Au, Ag and S elements were detectable. The overlays of different element mapping images show that these three elements were distributed uniformly throughout the whole Au–Ag_2S nanotrough because of its Au/Ag_2S core/shell-like architecture, which was further confirmed by the STEM-EDX linear scan element-distribution profile (Fig. S7, ESI†). Although the island-like particles show the typical lattice fringes of Ag_2S (Fig. 2b), the Au element was still detectable, as marked with the rectangular frame in Fig. 2c. The results indicate that some Au atoms penetrated the Ag_2S phase by diffusion because of the thermodynamic miscibility of Au and Ag_2S.[31,32] Combining TEM, HRTEM, and STEM-EDX elemental mapping analyses, we concluded that the Ag_2S layer in the Au–Ag_2S nanotrough wall was not pure Ag_2S, but rather a Ag_2S-rich mixture of Ag_2S and Au, as illustrated in Fig. 2d.

XRD characterization further confirmed that the AgAu nanotroughs were transformed into Au–Ag_2S nanotroughs (Fig. 3a). The 1D AgAu nanotrough has a face-centered cubic (fcc) structure with the diffraction peaks located at ~37.86, 44.12, 64.33 and 77.40°, corresponding to Ag- or Au(111), (200), (220) and (331) facets (Ag, PDF#65-8428; Au, PDF#04-0784), respectively. Additionally, the diffraction peak at 32.4° can be indexed to AgCl(200), suggesting the existence of some AgCl, similar to our previous work.[42] After sulfurization, many new diffraction peaks (Fig. 3a) were perfectly indexed to the monoclinic phase of Ag_2S(PDF#14-0072), and meanwhile, the Au diffraction peaks still remained, as marked with "∇", which was further confirmed by XPS analysis (Fig. 3b–d). Binding energies of Au–Ag_2S nanotroughs centered at ~84.09 and 87.76 eV (Fig. 3b) corresponded to $4f_{5/2}$ and $4f_{7/2}$ of Au^0, respectively.[32] The Ag $3d_{5/2}$ and $3d_{3/2}$ binding energies were ~367.5 and 373.5 eV, respectively (Fig. 3c), corresponding to Ag^+ of Ag_2S.[46] Also, each Ag 3d energy band was symmetric along the band center axis,

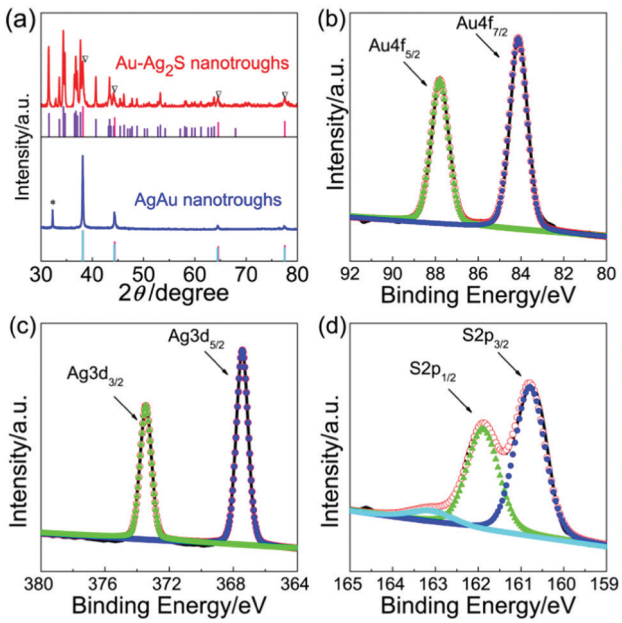

Fig. 2 STEM (a), TEM (b), HRTEM (b), and STEM-EDX mapping (c) images of 1D Au–Ag_2S nanotroughs; cartoon image (d) of a 1D Au–Ag_2S nanotrough and the illustration of its wall.

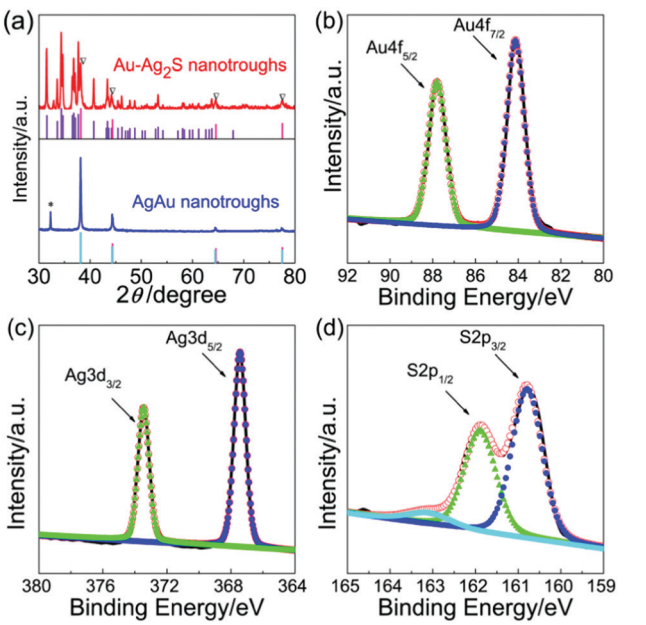

Fig. 3 (a) XRD patterns of 1D AgAu and Au–Ag_2S nanotroughs, together with the standard patterns of Ag (JCPDS#65-8428), Au (JCPDS#04-0784), and Ag_2S (JCPDS#14-0072). Peaks marked with "*" and "∇" in (a) are ascribed to AgCl and Au, respectively. (b)–(d) XPS spectra of the Au–Ag_2S nanotroughs: Au 4f (b), Ag 3d (c), and S 2p (d). The black solid curve and the red circle curve are the original and simulated curve, respectively, and the other symbol curves are the deconvoluted ones.

indicating that the Ag^0 of the AgAu nanotrough was converted to Ag^+. Furthermore, the $2p_{3/2}$ and $2p_{1/2}$ binding energies of S^{2-} were found to be located at ~160.7 and 161.9 eV (Fig. 3d), respectively,[47] confirming the formation of Ag_2S.

Besides, according to the XPS spectra, the Ag : S atomic ratio of the Au–Ag_2S nanotrough was calculated to be ~1.5 : 1, smaller than the chemically stoichiometric ratio of Ag_2S, 2 : 1, suggesting that there are more S^{2-} ions probably adsorbed on the exterior surface of Au–Ag_2S.[12] The as-formed Au–Ag_2S nanotrough not only had a unique nanostructure, but also exhibited strong absorption over a broad wavelength from 400 to 800 nm (Fig. 4a). The original Ag nanowires displayed two absorbance peaks at ~352 and 394 nm, ascribed to the out-of-plane quadrupole resonance and the transverse SPR of the Ag nanowires, respectively.[48,49] Compared to the original Ag nanowires, the 1D AgAu nanotroughs showed a broader absorption peak, the center of which was slightly red-shifted due to the intervention of Au,[50] similar to the spectrum behavior of the transformation from Ag nanowire to AgAu nanotube.[51] After the sulfurization, the characteristic absorption of the Ag nanowires completely disappeared, further indicating that the Ag^0 component had been transformed into Ag_2S.[32] According to a previous report,[49] pure Ag_2S nanowires do not have obvious absorption in the visible region. Therefore, the absorption of the 1D Au–Ag_2S nanotrough intrinsically originates from Au. Compared with that of the AgAu nanotrough, the enhanced absorption of the Au–Ag_2S nanotrough in the visible region may be attributed to the difference of dielectric constants between Ag_2S and Ag.[30,49] In addition, it is noted that the Au–Ag_2S nanohybrid showed decreased PL intensity (Fig. S8, ESI†) compared with pure Ag_2S, indicating that the introduction of Au can promote the separation of interfacial carriers.[18] This strong absorption in the visible region and lower PL intensity may enable the 1D Au–Ag_2S nanotroughs to exhibit visible-near-IR photoelectric activity.

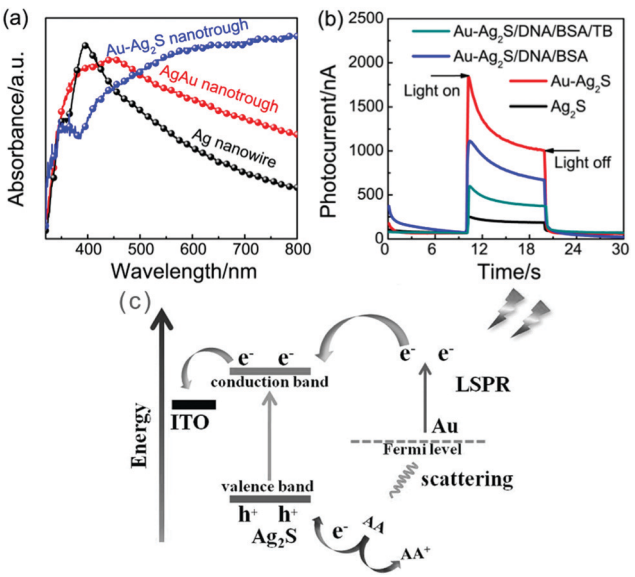

Fig. 4 (a) UV-vis absorption spectra of the Ag nanowire, AgAu, and Au–Ag_2S nanotroughs; (b) photocurrent responses of ITO/Ag_2S, ITO/Au–Ag_2S, ITO/Au–Ag_2S/DNA/BSA and ITO/Au–Ag_2S/DNA/BSA/TB in 0.10 mol L^{-1} Tris–HCl (pH 7.4) containing 0.10 mol L^{-1} ascorbic acid. ITO/Au–Ag_2S/DNA/BSA/TB was obtained by adding 20 μL of 10.0 pmol L^{-1} human α-thrombin onto ITO/Au–Ag_2S/DNA/BSA. (c) The photocurrent generation mechanism of the ITO/Au–Ag_2S electrode.

Under light irradiation (λ > 420 nm), the ITO/Au–Ag_2S electrode showed a favorable PEC response (Fig. 4b), the photocurrent of which (1718.3 nA) was about 8.5-fold higher than that of the ITO/Ag_2S electrode (203.5 nA). Particularly, due to the consumption of AA, the photocurrent decayed with the increase of the illumination time.[52,53] Moreover, the photocurrent was not significantly changed after 15 cycles (Fig. S9, ESI†), indicating that the 1D Au–Ag_2S nanotroughs had good stability during the tests. According to a previous investigation,[18] this enhanced PEC activity of Au–Ag_2S could be reasonably explained by the LSPR effect of Au (Fig. 4c) and the morphological feature: (1) the Ag_2S shell of Au–Ag_2S can be readily excited by incident light (λ > 420 nm),[30] resulting in the transfer of electrons from the valence band to the conduction band and thus generating e^-/h^+ pairs, and this excitation efficiency can be further improved by scattering light from Au.[54] (2) Meanwhile, the LSPR effect of Au generates energetic hot electrons on the surface of Au. These energetic electrons have more negative potential than the conduction band of Ag_2S,[55,56] and can transfer smoothly from Au to the conduction band of Ag_2S. (3) The enhanced localized electric field around Au also suppresses the recombination of generated e^-/h^+.[18] (4) The trough-like Au–Ag_2S nanostructure possesses a large specific surface area, favoring the enlargement of photocurrent signal. (5) The 1D morphology facilitates rapid and long-distance electron transfer.[34,35] (6) The Au/Ag_2S core/shell-like structure produces double hetero-junctions, shortening electron-transport distance and reducing the probability of e^-/h^+ recombination.[40] All the factors mentioned above may together contribute to a remarkable PEC response of the Au–Ag_2S nanotrough (Fig. 4b).

3.2 Application of Au–Ag_2S in a PEC sensor

Although ITO/Au–Ag_2S exhibited a satisfactory PEC response, whether this PEC response is effective enough for practical use is still a pending question. Therefore, we used ITO/Au–Ag_2S to construct a PEC sensor and assessed its sensing performance towards TB (Scheme 1). The as-fabricated bio-active PEC electrode (*i.e.*, ITO/Au–Ag_2S/DNA/BSA) showed a smaller photocurrent than that of ITO/Au–Ag_2S (Fig. 4b). When the targeted molecule, TB, bound with DNA of ITO/Au–Ag_2S/DNA/BSA, the photocurrent further decreased (Fig. 4b) because of the increase of the electron-transfer resistance (Fig. S10, ESI†).

Additionally, the photocurrent magnitude of ITO/Au–Ag_2S/DNA/BSA/TB closely depends on the TB concentrations. To establish the correlation between the photocurrent and TB concentration, we used TB of different concentrations to fabricate ITO/Au–Ag_2S/DNA/BSA/TB electrodes (see Experimental section). Fig. 5a shows the photocurrents of ITO/Au–Ag_2S/DNA/BSA/TB with different concentrations of TB. Obviously, the higher the TB concentration, the smaller the photocurrent. The photocurrent *versus* TB concentration plot had a good

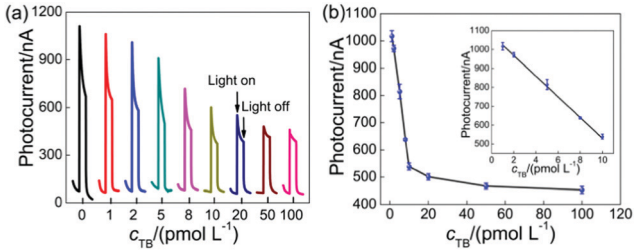

Fig. 5 (a) Photocurrent responses of the ITO/Au–Ag_2S/DNA/BSA electrode to TB of different concentrations (c_{TB}) in 0.10 mol L^{-1} Tris–HCl (pH 7.4) containing 0.10 mol L^{-1} ascorbic acid; (b) calibration curves of *I versus* c_{TB}. Inset of (b) is the linear correlation plot at the TB concentration ranging from 1.00 to 10.00 pmol L^{-1}.

linear relation over the range from 1.00 to 10.00 pmol L^{-1} (Fig. 5b). The detection limit was calculated to be ~0.67 pmol L^{-1} based on the 3σ method, better than those of previous reports (Table S1, ESI†).

3.3 Selectivity, reproducibility, stability and applicability of the PEC sensor

Moreover, the as-fabricated bio-active ITO/Au–Ag_2S/DNA/BSA electrode also had excellent selectivity towards TB. Among six examined proteins, that is, alkaline phosphatase (ALP), lysozyme, glucose oxidase (GO_x), pepsin, BSA and TB, TB exhibited the strongest specific interaction with the ITO/Au–Ag_2S/DNA/BSA electrode and thus dramatically reduced the photocurrent. The photocurrent variation caused by all the proteins, ΔI, is shown in Fig. 6a. Although the concentration of the interfering proteins (100.00 ng mL^{-1}) was much higher than that of TB (3.75 ng mL^{-1}), no substantial photocurrent reduction was observed after the ITO/Au–Ag_2S/DNA/BSA electrode was incubated with each interfering protein. To further verify the selectivity, we measured the response of the ITO/Au–Ag_2S/DNA/BSA electrode in a mixture of ALP, lysozyme, GO_x, pepsin, BSA and TB (Fig. 6a), and the result reveals that the photocurrent response towards the mixture is almost the same as that towards the TB solution, corroborating the excellent selectivity of ITO/Au–Ag_2S/DNA/BSA for TB detection.

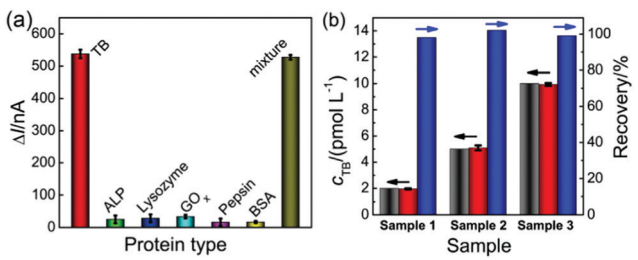

Fig. 6 (a) Photocurrent variations of ITO/Au–Ag_2S/DNA/BSA in 0.10 mol L^{-1} Tris–HCl (pH 7.4) containing 0.10 mol L^{-1} ascorbic acid after the interaction with each protein (TB, ALP, lysozyme, GO_x, pepsin, or BSA) and their mixture. Except for TB whose concentration was 10.0 pmol L^{-1} (*i.e.*, 3.75 ng mL^{-1}), the other proteins were fixed at a concentration of 100.00 ng mL^{-1}. (b) Recovery assay of TB of different concentrations (c_{TB}) in human serum sample diluted 10-fold by 10.0 mmol L^{-1} phosphate buffer saline (PBS) (pH 7.4): sample 1, 2.0 pmol L^{-1}; sample 2, 5.0 pmol L^{-1}; sample 3, 10.0 pmol L^{-1}.

Additionally, the ITO/Au–Ag_2S/DNA/BSA electrode exhibited good reproducibility and stability. Five electrodes prepared separately under the same conditions were used to detect TB (10.0 pmol L^{-1}), and the relative standard deviation (RSD) was only ~4.3%. The photocurrent could retain ~94.1% of its initial value for TB detection after 2 weeks of storage in a refrigerator at 4 °C. In order to verify the applicability and reliability of the ITO/Au–Ag_2S/DNA/BSA electrode, we further detected different concentrations of TB in the 10-fold diluted human blood serum samples (diluted with 10 mmol L^{-1} PBS, pH 7.4). The TB recoveries were up to 98%, 102%, and 99% for 2, 5, and 10 pmol L^{-1} TB, respectively (Fig. 6b), indicating that ITO/Au–Ag_2S/DNA/BSA can be used for TB detection of real samples.

4 Conclusions

We obtained 1D Au–Ag_2S nanotroughs by using Ag nanowires as raw materials involving interfacial self-assembly of Ag nanowires, site-specific etching of interfacial Ag nanowires with $AuCl_4^-$, and sulfurization by S^{2-}. The wall of the 1D Au–Ag_2S nanotrough had a Au/Ag_2S core/shell-like architecture. The Au–Ag_2S nanotrough showed enhanced absorption in the visible-near-infrared region and exhibited excellent photoactive performance because of the LSPR effect of Au and its 1D morphological feature. The PEC biosensor based on the 1D Au–Ag_2S nanotroughs showed excellent analytical performance for TB with a sensitive linear response ranging from 1.00 to 10.00 pmol L^{-1} and a low detection limit of 0.67 pmol L^{-1}. Also, the PEC biosensor possessed high selectivity, satisfactory reproducibility and good stability. This study provides some insight into the enhancement of plasmonic metals towards PEC activity, and also the Au–Ag_2S nanotrough may have other promising applications in areas such as photocatalysis and photovoltaics.

Conflicts of interest

There are no conflicts to declare.

Acknowledgements

This study was financed by National Natural Science Foundation of China (no. 21872048 and 21703013).

References

1 W. W. Zhao, J. J. Xu and H. Y. Chen, *Chem. Rev.*, 2014, **114**, 7421–7441.
2 X. R. Zhang, M. S. Liu, H. X. Liu and S. S. Zhang, *Biosens. Bioelectron.*, 2014, **56**, 307–312.
3 Z. Y. Wang, J. Liu, X. Liu, X. Y. Shi and Z. H. Dai, *Anal. Chem.*, 2019, **91**, 830–835.
4 S. S. Liu, H. J. Cao, X. Y. Wang, W. W. Tu and Z. H. Dai, *Nanoscale*, 2018, **10**, 16474–16478.

5 D. W. Fan, C. Z. Bao, X. Liu, D. Wu, Y. Zhang, H. Wang, B. Du and Q. Wei, *J. Mater. Chem. B*, 2018, **6**, 7634–7642.
6 W. W. Tu, J. P. Lei, P. Wang and H. X. Ju, *Chem. – Eur. J.*, 2011, **17**, 9440–9447.
7 J. Y. Zhuang, W. Q. Lai, M. D. Xu, Q. Zhou and D. P. Tang, *ACS Appl. Mater. Interfaces*, 2015, **7**, 8330–8338.
8 J. Tian, Y. H. Leng, Z. H. Zhao, Y. Xia, Y. H. Sang, P. Hao, J. Zhan, M. C. Li and H. Liu, *Nano Energy*, 2015, **11**, 419–427.
9 W. L. Yu, D. F. Xu and T. Y. Peng, *J. Mater. Chem. A*, 2015, **3**, 19936–19947.
10 J. L. Wang, R. A. Ando and P. H. C. Camargo, *Angew. Chem., Int. Ed.*, 2015, **127**, 7013–7016.
11 T. H. Yang, L. D. Huang, Y. W. Harn, C. C. Lin, J. K. Chang, C. I. Wu and J. M. Wu, *Small*, 2013, **9**, 3169–3182.
12 S. C. Han, L. F. Hu and N. Gao, *Adv. Funct. Mater.*, 2014, **24**, 3725–3733.
13 R. Shi, Y. H. Cao, Y. J. Bao, Y. F. Zhao, G. I. N. Waterhouse, Z. Y. Fang, L. Z. Wu, C. H. Tung, Y. D. Yin and T. R. Zhang, *Adv. Mater.*, 2017, **29**, 1700803.
14 J. S. Lee, E. V. Shevchenko and D. V. Talapin, *J. Am. Chem. Soc.*, 2008, **130**, 9673–9675.
15 M. S. Wu, L. J. He, J. J. Xu and H. Y. Chen, *Anal. Chem.*, 2014, **86**, 4559–4565.
16 R. B. Jiang, B. X. Li, C. H. Fang and J. F. Wang, *Adv. Mater.*, 2014, **26**, 5274–5309.
17 X. C. Ma, H. Sun, Y. C. Wang, X. Wu and J. Q. Zhang, *Nano Energy*, 2018, **53**, 932–939.
18 R. Y. Li, W. W. Tu, H. S. Wang and Z. H. Dai, *Anal. Chem.*, 2018, **90**, 9403–9409.
19 S. K. Dutta, S. K. Mehetor and N. J. Pradhan, *Phys. Chem. Lett.*, 2015, **6**, 936–944.
20 S. K. Cushing, J. T. Li, J. Bright, B. T. Yost, P. Zheng, A. D. Bristowand and N. Q. Wu, *J. Phys. Chem. C*, 2015, **119**, 16239–16244.
21 X. T. Wang, C. C. Liow, D. P. Qi, B. W. Zhu, W. R. Leow, H. Wang, C. Xue, X. D. Chen and S. Z. Li, *Adv. Mater.*, 2014, **26**, 3506–3512.
22 J. Kolny-Olesiak and H. Weller, *ACS Appl. Mater. Interfaces*, 2013, **5**, 12221–12237.
23 J. Li, X. F. Lin, Z. Y. Zhang, W. W. Tu and Z. H. Dai, *Biosens. Bioelectron.*, 2019, **126**, 332–338.
24 W. L. Yang, L. Zhang, Y. Hu, Y. J. Zhong, H. B. Wu and X. W. Lou, *Angew. Chem., Int. Ed.*, 2012, **124**, 11669–11672.
25 C. X. Wang, Y. Wang, L. Xu, D. Zhang, M. X. Liu, X. W. Li, H. C. Sun, Q. Lin and B. Yang, *Small*, 2012, **8**, 3137–3142.
26 C. H. Lu, G. H. Chen, B. Yu and H. L. Cong, *Adv. Eng. Mater.*, 2018, **20**, 1700940.
27 L. L. Dong, G. M. Ji, Y. Liu, X. Xu, P. P. Lei, K. M. Du, S. Y. Song, J. Feng and H. J. Zhang, *Nanoscale*, 2018, **10**, 825–831.
28 M. M. Shahjamali, Y. Zhou, N. Zaraee, C. Xue, J. S. Wu, N. Large, C. M. McGuirk, F. Boey, V. Dravid, Z. F. Cui, G. C. Schatz and C. A. Mirkin, *ACS Nano*, 2016, **10**, 5362–5373.
29 B. Liu and Z. F. Ma, *Small*, 2011, **7**, 1587–1592.
30 Z. Z. Lou, S. Kim, M. Fujitsuka, X. G. Yang, B. J. Li and T. Majima, *Adv. Funct. Mater.*, 2018, **28**, 1706969.
31 J. Yang and J. Y. Ying, *J. Am. Chem. Soc.*, 2010, **132**, 2114–2115.
32 L. Xu, Z. Y. Yin, S. W. Cao, Z. X. Fan, X. Zhang, H. Zhang and C. Xue, *Chem. – Eur. J.*, 2014, **20**, 2742–2745.
33 Q. Cao and R. C. Che, *ACS Appl. Mater. Interfaces*, 2014, **6**, 7020–7027.
34 Z. R. Tang, X. Yin, Y. H. Zhang and Y. J. Xu, *Inorg. Chem.*, 2013, **52**, 11758–11766.
35 H. Dai, Y. L. Li, S. P. Zhang, L. S. Gong, X. H. Li and Y. Y. Lin, *Sens. Actuators, B*, 2016, **222**, 120–126.
36 S. Q. Liu, Z. R. Tang, Y. G. Sun, J. C. Colmenares and Y. J. Xu, *Chem. Rev.*, 2015, **44**, 5053–5075.
37 F. Nan, S. Liang, J. H. Wang, X. L. Liu, D. J. Yang, X. F. Yu, L. Zhou, Z. H. Hao and Q. Q. Wang, *Adv. Opt. Mater.*, 2014, **2**, 679–686.
38 J. L. Qu, H. Liu, Y. F. Wei, X. F. Wu, R. L. Yue, Y. F. Chen and J. Yang, *J. Mater. Chem.*, 2011, **21**, 11750–11753.
39 Y. G. Hu, C. Gao and Y. J. Xiong, *Dalton Trans.*, 2018, **47**, 12035–12040.
40 J. D. Xiao, L. L. Han, J. Luo, S. H. Yu and H. L. Jiang, *Angew. Chem., Int. Ed.*, 2018, **57**, 1103–1107.
41 H. Y. Shi, B. Hu, X. C. Yu, R. L. Zhao, X. F. Ren, S. L. Liu, J. W. Liu, M. Feng, A. W. Xu and S. H. Yu, *Adv. Funct. Mater.*, 2010, **20**, 958–964.
42 W. C. Geng, W. J. Shen, H. H. Xue, J. L. Sang, L. N. Zhou, X. Yin and Y. J. Li, *ChemNanoMat*, 2019, **5**, 208–214.
43 H. H. Xue, W. J. Shen, W. C. Geng, X. Yin, Y. Yang, S. Guo and Y. J. Li, *Chem. Commun.*, 2018, **54**, 7227–7230.
44 Y. J. Li, W. J. Huang and S. G. Sun, *Angew. Chem., Int. Ed.*, 2006, **45**, 2537–2539.
45 C. H. Fang, Y. H. Lee, L. Shao, R. B. Jiang, J. F. Wang and Q. H. Xu, *ACS Nano*, 2013, **7**, 9354–9365.
46 M. L. Pang, J. Y. Hu and H. C. Zeng, *J. Am. Chem. Soc.*, 2010, **132**, 10771–10785.
47 G. S. Li, L. Wu, F. Li, P. P. Xu, D. Q. Zhang and H. X. Li, *Nanoscale*, 2013, **5**, 2118–2125.
48 M. S. Goh, Y. H. Lee, S. Pedireddy, I. Y. Phang, W. W. Tjiu, J. M. R. Tan and X. Y. Ling, *Langmuir*, 2012, **28**, 14441–14449.
49 N. Du, H. Zhang, H. Sun and D. Yang, *Mater. Lett.*, 2007, **61**, 235–238.
50 N. R. Sieb, N. C. Wu, E. Majidi, R. Kukreja, N. R. Branda and B. D. Gates, *ACS Nano*, 2009, **3**, 1365–1372.
51 Y. G. Sun and Y. N. Xia, *J. Am. Chem. Soc.*, 2004, **126**, 3892–3901.
52 R. Y. Yang, Y. M. Li, K. Zou, L. X. Meng, X. H. Zhang and J. H. Chen, *Chem. Commun.*, 2018, **54**, 4830–4833.
53 J. G. Yu and B. Wang, *Appl. Catal., B*, 2010, **94**, 295–302.
54 S. K. Cushing, J. T. Li, F. K. Meng, T. R. Senty, S. Suri, M. J. Zhi, M. Li, A. D. Bristow and N. Wu, *J. Am. Chem. Soc.*, 2012, **134**, 15033–15041.
55 J. Shu, Z. L. Qiu, S. Z. Lv, K. Y. Zhang and D. P. Tang, *Anal. Chem.*, 2018, **90**, 2425–2429.
56 R. Y. Li, R. Yan, J. C. Bao, W. W. Tu and Z. H. Dai, *Chem. Commun.*, 2016, **52**, 11799–11802.